







Cite this: *Lab Chip*, 2021, 21, 1563

# Controlled orientation and sustained rotation of biological samples in a sono-optical microfluidic device†

Mia Kvåle Løvmo,  Benedikt Pressl,   
 Gregor Thalhammer  and Monika Ritsch-Marte \*

In cell biology, recently developed technologies for studying suspended cell clusters, such as organoids or cancer spheroids, hold great promise relative to traditional 2D cell cultures. There is, however, growing awareness that sample confinement, such as fixation on a surface or embedding in a gel, has substantial impact on cell clusters. This creates a need for contact-less tools for 3D manipulation and inspection. This work addresses this demand by presenting a reconfigurable, hybrid sono-optical system for contact-free 3D manipulation and imaging, which is suitable for biological samples up to a few hundreds of micrometers in liquid suspension. In our sono-optical device, three independently addressable MHz transducers, an optically transparent top-transducer for levitation and two side-transducers, provide ultrasound excitation from three orthogonal directions. Steerable holographic optical tweezers give us an additional means of manipulation of the acoustically trapped specimen with high spatial resolution. We demonstrate how to control the reorientation or the spinning of complex samples, for instance for 3D visual inspection or for volumetric reconstruction. Whether continuous rotation or transient reorientation takes place depends on the strength of the acoustic radiation torque, arising from pressure gradients, compared to the acoustic viscous torque, arising from the shear forces at the viscous boundary layer around the particle. Based on numerical simulations and experimental insights, we develop a strategy to achieve a desired alignment or continuous rotation around a chosen axis, by tuning the relative strengths of the transducers and thus adjusting the relative contributions of viscous and radiation torques. The approach is widely applicable, as we discuss in several generic examples, with limitations dictated by size and shape asymmetry of the samples.

Received 11th December 2020,  
 Accepted 28th January 2021

DOI: 10.1039/d0lc01261k

[rsc.li/loc](http://rsc.li/loc)

## 1 Introduction

In the life sciences it is increasingly acknowledged that the properties of complex living specimens cannot be understood solely on the single cell level, because interactions with neighbouring cells play a crucial role. With the recent rise of cancer spheroid and organoid technology,<sup>1–3</sup> it has been possible to perform *in vitro* research that extends beyond cell cultures and closes the gap to *in vivo* studies. In this context, it is important to provide a natural environment and to avoid contact with surfaces. The quest for fixation-free and contact-less manipulation tools for complex live biological samples is more important than ever.

Ashkin's optical tweezers,<sup>4,5</sup> particularly in the form of holographically shaped and steered tweezers,<sup>6–9</sup> provide a versatile tool to accomplish this goal. Dielectric particles in water solution can be held, moved, or rotated in a contact-free way in holographically reconfigurable trapping landscapes. Yet, optical trapping has its limitations: for large and heavy multi-cellular specimens the application of single-beam optical tweezers becomes problematic, because the required optical powers to create sufficiently strong forces may give rise to photodamage. This limit can be extended towards larger objects with optical 'macro-tweezers',<sup>10</sup> a specially designed optical dual-beam mirror-trap with large field-of-view and trapping volume. With this device it was possible to hold, *e.g.*, swimming micro-organisms of ~70 µm length and to force them on a trajectory with forces exceeding 100 pN with minor temperature rise (contrary to what is sometimes stated in the literature<sup>11</sup>). But for significantly larger organisms this approach also reaches its limits.

This is where acoustic trapping in liquids becomes an interesting alternative.<sup>12</sup> Coupling acoustic waves into the

Institut für Biomedizinische Physik, Medizinische Universität Innsbruck,  
 Müllerstraße 44, 6020 Innsbruck, Austria.  
 E-mail: [monika.ritsch-marte@i-med.ac.at](mailto:monika.ritsch-marte@i-med.ac.at); Fax: +43 512 9003 73871;  
 Tel: +43 512 9003 70871

† Electronic supplementary information (ESI) available: Including Movies S1–S10. See DOI: 10.1039/d0lc01261k



sample solution causes pressure changes in the fluids, which result in the well-known acoustic radiation forces.<sup>13</sup> At frequencies of a few MHz, the wavelength in water is a few 100  $\mu\text{m}$ , which gives strong forces on samples of the same size scale, with very low impact on the viability of living specimens.<sup>14</sup>

Compared to optics, the spatial resolution of acoustic trapping is reduced due to the larger wavelength. Nevertheless, in acoustics an impressively high level of control of positioning can be reached, *e.g.*, by employing surface acoustic standing waves,<sup>15,16</sup> also with dynamic shaping.<sup>17,18</sup> Also, phased-array emitters around a liquid-filled chamber<sup>19</sup> or diffractive beam shaping,<sup>20</sup> are employed, for instance for cell-sorting,<sup>21</sup> or patterning in ultrasonic gels.<sup>22</sup> Taking holographic optical tweezers (HOT) as a model, holographic acoustic tweezers (HAT) enable control of individual particles levitated in water<sup>23</sup> or air.<sup>24</sup> For the relatively large samples considered here, it is advantageous to use a simpler approach based on bulk acoustic waves rather than surface acoustic waves, since larger specimen size requires larger chamber volumes.<sup>25</sup> Moreover, we are aiming at full 3D flexibility in the manipulation, far away from any surface and with *independent* control of all directions.

An example of a large living specimen which can be trapped acoustically, but not optically, is the tardigrade (*Hypsibius dujardini*), known colloquially as water bear or moss piglet, shown in Fig. 1 and ESI† Movie S1. This specimen, which measures about 190  $\mu\text{m}$  by 50  $\mu\text{m}$  in size, clearly would be beyond trapping with optical tweezers.

As the two physical trapping mechanisms complement each others strengths and weaknesses,<sup>12</sup> it is obviously highly advantageous to combine them in a single device: holographic optical tweezers operate on a finer scale, while the ultrasound can do the heavy lifting, quite literally. We follow the suggestion of Memoli and Fury,<sup>26</sup> and name this combination of acoustic and optical trapping a ‘sono-optical’ device, in order to avoid confusion with acousto-optics or photo-acoustics. We expect a benefit from such devices in the precise handling and inspection of large (>100  $\mu\text{m}$ ) living specimens, such as microorganisms, embryos, cancer spheroids, or organoids. One would like to keep complex samples in a natural environment, unhampered by confining structures (*e.g.*, when embedded in gel) or walls (*e.g.*, when stored in micro-well plates or squeezed between glass slides), especially for long term monitoring.

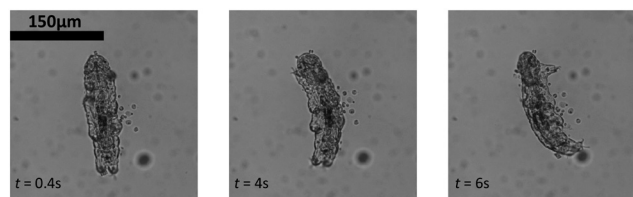


**Fig. 1** Acoustic trapping of a large and actively moving live specimen: a tardigrade or ‘moss piglet’ is levitated and confined in 3D (ESI† Movie S1).

In our previous work we demonstrated such sono-optical devices for the first time, combining acoustic levitation with optical macro-tweezers,<sup>68</sup> and later with single beam holographic optical tweezers. In both cases acoustics were mostly used for levitating particles against gravity within a plane, and optical manipulation for precise control within this plane. This approach also opens the path to high-quality optical imaging of levitated trapped specimens and detailed measurements of acoustic forces.<sup>27–29</sup> Hybrid sono-optical chips may profit from complementary features of the two modalities,<sup>30</sup> which has, *e.g.*, been utilized for improving the separation of sub-populations of white blood cells based on differences in both, mechanical and optical properties.<sup>31</sup>

When aiming at the manipulation of specimens of increasing size, of 100  $\mu\text{m}$  or more in diameter, one faces new challenges, which we have tackled in this work:

- For increasing specimen size, holographic optical tweezers lose their dominant role over acoustics, and it becomes desirable to have more flexibility in the acoustic forces. Therefore, going beyond the simple 1D standing wave used previously, we have implemented 3D acoustic trapping with three independent transducers for each of the three orthogonal directions.
- As the size (and shape) of the device needs to be scaled to accommodate larger samples, the acoustic modes inside the up-scaled 3D acoustic trapping device are affected and more complex patterns appear, which required investigation in theory and experiment.
- For large samples, retrieving knowledge of the 3D structure is problematic, as standard microscopic imaging is hampered by the specimen itself. When focusing deep into the sample the image quality is degraded due to scattering, absorption, and particle induced aberrations. A simple approach to obtain 3D information is to rotate the particles (and not the imaging system) to obtain images from different viewing directions for optical tomographic imaging, using the extended micro-manipulation possibilities provided by our sono-optical trapping device.
- Acoustic trapping acts on a relatively large spatial scale compared to optical manipulation. Therefore, in our device we have implemented auxiliary holographic optical tweezers. The fact that the ‘heavy weight lifting’ is accomplished by the acoustic fields facilitates their usage, since the optical traps can be switched on and off at ease without ever losing stable trapping conditions for the sample. With this, (re-) positioning can be done on a scale much smaller than the typical acoustic wavelengths or particle sizes we use.

As a major contribution, we report observation of controlled reorientation and controlled continuous rotation of specimens in our devices, either when using only acoustics, or triggered by optical manipulation. We also present practical considerations to enable productive use in research.

The manuscript is organized as follows: sec. 2 explains the design, assembly, and properties of the microfluidic chambers. It is followed by sec. 3, a brief summary of the



relevant phenomena giving rise to acoustic torque on a particle. Sec. 4 explains the general strategies to induce rotations and exemplifies our experimental results on the controlled reorientation and the sustained rotation of various specimens.

## 2 Design, implementation, and characterization of the device

In this section we describe the design considerations, the manufacturing, and the characterization of the properties of our sono-optical manipulation device, a schematic sketch of which is shown in Fig. 2. We prefer flexible designs to enable easy adaption and tailoring for the specific needs of various applications, using standard components and equipment.

### 2.1 Outline of the setup for sono-optical manipulation

The centerpiece of our device supporting combined acoustic and optical manipulation is a mm-sized chamber, formed by machining a through-hole into a plate of acoustically hard material, which acts as an acoustic resonator. We rely on resonantly enhanced waves in the cavity, which is filled with water or a buffer solution, to achieve sufficiently strong acoustic forces. Fig. 3 shows images of some sono-optical devices we have used.

Three individually driven orthogonal transducers allow us to independently control the strength of the acoustic confinement in all directions. We preferably select bulk acoustic waves with clear directionality, to obtain good independent control. In the vertical direction we require the

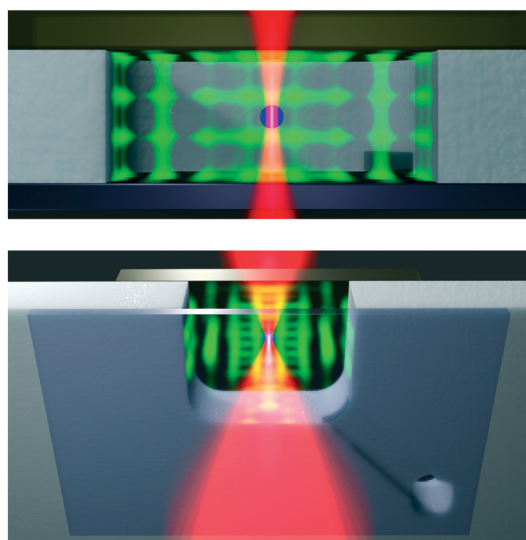


**Fig. 2** Sketch of the hybrid sono-optical device (not to scale), visualizing the acoustic force field (green), and the laser for optical manipulation (red). Top: View into the probe chamber along the horizontal plane. Bottom: View from below (with some parts cut away to expose a cross-section), showing the cover glass, the chip with acoustic resonator cavity and microfluidic channels, and the transparent ultrasound transducer.

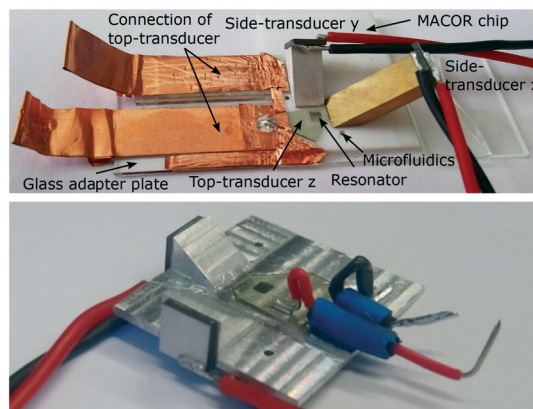


**Fig. 3** Images of assembled sono-optical devices. Top: Assembly based on ceramic plate with side-transducers mounted on metal wedges. Bottom: Monolithic design made of metal.

strongest confinement to hold particles against gravity. To achieve this, we place an ultrasound transducer made out of lithium niobate ( $\text{LiNbO}_3$ ) in direct contact with the fluid on top of the chamber, which provides good coupling for the ultrasound wave. A microscope cover slip on the bottom side seals the chamber and acts as a reflector for the acoustic wave. To excite the ultrasound wave in the horizontal directions we use side-transducers mounted on metal wedges glued to the base device substrate (see upper image in Fig. 3), or, in a monolithic design, attached to tapered metal structures, see lower image in Fig. 3.

The optically transparent  $\text{LiNbO}_3$  top-transducer provides very good optical access to the chamber,<sup>32</sup> supporting optical trapping and imaging. Moreover, the chip is designed to be fully compatible with standard microscopy setups, *i.e.*, it easily fits into an inverted microscope, which we use for standard wide-field imaging. More details about imaging and the details of the optical trapping are described in ESI† S1 and the optical setup is shown in ESI† Fig. S1.

### 2.2 Manufacturing and assembly of the sono-optical device

**2.2.1 Acoustic resonator.** We have fabricated several devices such as the ones shown in Fig. 3. They all follow the same general layout: in a 1 mm thick plate, a central through-hole of about 2 mm × 2 mm acts as acoustic resonator. The transverse cross-section of the chamber has an approximately rectangular shape, with rounded corners resulting from the milling. We have chosen a rectangular, not square, cross-section in our prototype in order to have clearly distinguishable resonances in each direction, as this eases individual excitation. As the material we use Macor, a machinable glass-ceramic with high inertness, or substitute it by aluminum (type 3.3547) for prototyping, which is easier to machine and of lower cost. Both materials have similar bulk-wave acoustic properties.

Surface-milled channels at the bottom side (width 1 mm, depth 300 μm) connect to opposing diagonal corners of the



chamber and act as inlet and outlet for filling the chamber. The channels end in 1 mm diameter through-holes, which provide a water-tight connection to standard pipette tips. On the bottom side, chamber and channels are sealed with a square 0.17 mm thick coverslip with a side length of 20 mm. The layout is simple enough so that hand-milling with a single 1 mm diameter tool is feasible and efficient.

**2.2.2 Ultrasound transducers.** A transducer made of optical grade LiNbO<sub>3</sub> (36° Y-cut, 0.5 mm or 1 mm thickness, Roditi) with transparent ITO electrodes (sheet resistance 10 Ω sq<sup>-1</sup>, Diamond Coatings) covers the top of the chamber. Ultrasound from the sides is generated by standard piezo plates (6 mm × 6 mm, 1 mm thick, material type Pz26, Meggitt) with silver electrodes. As it is impractical to attach sufficiently large transducers directly to the sides of a thin substrate, we explored two alternatives to couple the ultrasound into the resonator chamber. First, as seen in Fig. 3 top panel, we followed the design from Manneberg *et al.*<sup>33</sup> and used brass or aluminium wedges between piezo-plates and chip carrier with a wedge-angle semi-empirically chosen. We have performed simple bulk wave simulations to choose the optimal wedge-angle, but realized that the glue interfaces between piezo, wedge and chip carrier are more of a limiting factor with regards to coupling efficiency at this stage. As an alternative approach, we also use tapered structures in a monolithic chip carrier design, as shown in the lower part of Fig. 3, which avoids reflection at one interface between different materials and also avoids reducing transmission of the acoustic wave by one glue interface. Hence, the monolithic design yields stronger forces from the side-transducers relative to the wedge-based design.

**2.2.3 Assembly of the device.** For the prototype devices, the assembly is made reversible, which enables us to flexibly rework just some components, without the need for complete disassembly. Most often we want to remove the cover glass for cleaning the chamber. We use a thin layer of petroleum jelly (Vaseline) to form a water-tight seal between the cover glass and the bottom of the chip carrier, which allows for an easy removal. To interface the transducers, wedges, and chip-carrier, we use hot glue (CrystalBond 509), which melts when heated above 90°. Alternatively we use cyanoacrylate glue, which is removable by exposure to solvents such as acetone. For the electrical connections to the ITO coated transparent transducer, we use silver paint (RS: 123-9911) to assure good electrical connection to copper wires or foil (35 μm thickness with adhesive coating). The PZT transducers, which have silver plated electrodes, are connected with a standard, low-temperature hand-soldering process (Sn<sub>60</sub>Pb<sub>40</sub> solder) to copper wires.

## 2.3 Acoustic resonator modes and trapping landscape

In order to excite independent standing waves in all directions to obtain a 3D acoustic confinement with individual control of the trapping strength in all directions, our design employs separate plate transducers operating in

thickness vibration mode that by their own generate plane acoustic waves. However, as we rely on acoustic resonances within the probe chamber to boost the force strength, primarily the geometry of the acoustic resonator determines the shape of the acoustic resonance modes. Therefore we chose an approximately cuboid shape for our probe chamber, which—in the ideal case—supports standing plane waves in each direction.<sup>34</sup>

Since the fabricated chamber has a horizontal cross-section with rounded corners and thus deviates from a perfect cuboid, we have carried out simulations based on finite element methods (FEM) in order to get a general idea of the modes in our chamber. For this we look into the solutions of the wave equation

$$\nabla^2 p - \frac{1}{c^2} \frac{\partial^2 p}{\partial t^2} = 0 \quad (1)$$

for ultrasound waves in the resonator. Here,  $p$  denotes the sound pressure, and  $c$  the speed of sound in the medium (water  $c = 1490$  ms). We assume hard wall boundary conditions.<sup>34</sup> To numerically find solutions for the eigenmodes we employ finite element methods using Mathematica for 2D simulations, and SfePy for 3D simulations. In the following we present mostly results for purely horizontal modes, *i.e.*, modes without nodes along the vertical direction.

**2.3.1 Modes along the vertical direction.** Standing waves in the vertical  $z$ -direction in a similar system have already been studied in detail in our previous work.<sup>27</sup> As already expected from basic theory,<sup>34</sup> the sound pressure amplitude  $p$  varies sinusoidally with the vertical position, with a maximum close to the (hard wall) boundaries between water and cover glass/transducer. The acoustic radiation force, which is approximately proportional to the gradient of the squared sound pressure,  $F \propto \nabla p^2$ , also varies sinusoidally and pushes particles to planes (pressure nodes) repeated at distances of  $\lambda/2$ , with the lowest node at about  $\lambda/4$  from the bottom. Typically, we drive the vertical transducer at frequencies close to its fundamental thickness resonance, which for a 0.5 mm and 1 mm thick LiNbO<sub>3</sub> plate is at about 6.6 MHz and 3.3 MHz respectively. In a 1 mm thick water filled probe chamber the latter frequency creates 5 nodal planes, where particles are stably levitated, with a vertical spacing of  $\lambda/2 \approx 200$  μm.

**2.3.2 Modes along the horizontal direction.** Similar considerations apply to the force landscape in the horizontal directions. The side-transducers we use are 1 mm thick piezo-plates (see also sec. 2.2) with a fundamental resonance frequency around 2 MHz. In our chamber of dimensions  $L_x = 2.690$  mm and  $L_y = 2.487$  mm we can, for instance, excite a resonance at 2.2 MHz, which accommodates 8 lateral nodes with a spacing of about 340 μm in  $L_x$ . Due to manufacturing by milling, the acoustic resonator has rounded corners in the  $xy$ -plane with a radius of 0.5 mm. This affects the standing wave patterns at resonance, which are not plane waves anymore, leading to an altered force landscape compared to





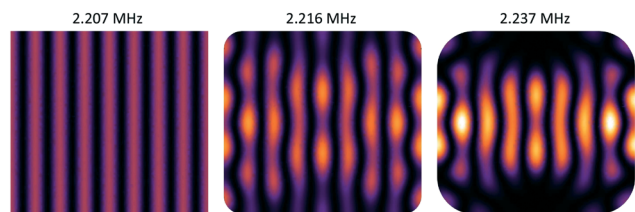


**Fig. 4** Acoustic eigenmodes for a 2.5 mm  $\times$  2.7 mm resonator with hard wall boundary conditions. Color encodes  $p^2$ , which approximately gives the acoustic force potential. Typically particles are trapped at the minima (black regions). Shown are the results for different corner roundings; from left to right: square corners,  $r_0 = 0.25$  mm, and  $r_0 = 0.5$  mm (our experimental case).

a design with square corners. This is shown in Fig. 4, for a chamber with dimension 2.5 mm by 2.7 mm, which approximates our experimental condition. When changing the corner style from sharp to rounded, the trapping nodes change from perfectly straight lines to bent, wavy lines.

**2.3.3 3D acoustic trapping.** The use of three independent transducers provides us with an enhanced flexibility for creating acoustic trapping landscapes in 3D. When we simultaneously drive all transducers to excite the respective dominant resonance in each direction, in principle, interference between the individual acoustic waves also affects the acoustic forces. However, since the resonance frequencies differ significantly, the contributions from interference terms oscillate at a fast rate and their effects on the acoustic forces average out. The total combined acoustic trapping potential is the mere sum of the individual potentials.

By tuning the individual voltages of the transducers one can control the pattern. Driving a single transducer excites a roughly planar wave, while exciting all three transducers confines particles to well separated trapping spots arranged in a more or less regular grid. We prefer this configuration for trapping of large, living specimens. Each trapping site provides a 3D confinement, where the trap stiffness along each direction can be controlled individually. As we will demonstrate in sec. 4.1, this allows us to control the orientation of trapped particles.

But even when we drive a single transducer, we observe some 3D confinement, *e.g.*, additional weaker forces acting in the horizontal direction, when only the top-transducer is actuated. Furthermore, we observe some deviation of the vertical trapping position with horizontal position from an ideal flat arrangement. As our 3D simulations indicate, we attribute this to a simultaneous excitation of more than a single mode by the top-transducer, including modes with nodes along the horizontal directions, which is facilitated by small asymmetries in our actual resonator. Our calculations predict a quite dense set of modes, with unequal frequency spacing of the resonances with a mean value of 6 kHz and a maximum of 20 kHz in the range of 2 MHz to 2.4 MHz for the 3D case. Due to this dense spacing it is likely to excite several resonances, which are observed to have a width of several kHz. We suppose that this simultaneous excitation of

at least two modes by a single frequency is a key ingredient to induce sustained rotation by a mechanism which we discuss in sec. 3.

In cases when we prefer flatter, more uniform horizontal confinement layers from the top-transducer, we sometimes additionally apply frequency dithering to the top-transducer. For this we rapidly modulate the excitation frequency, with frequency deviation of 50 kHz at a rate of 1 kHz. This simultaneously excites several neighbouring acoustic modes within a bandwidth of about 100 kHz with strongly varied phase relations. Individual differences in the trapping landscape are averaged out, which leads to more regular and uniform trapping. Furthermore, the sensitivity to small changes of the resonance frequencies, *e.g.*, due to temperature changes, is reduced.

## 2.4 Experimental characterization of acoustic resonances

Since the resonance frequencies are rather sensitive to small variation in the actual settings, we always determine the precise resonance frequencies experimentally, to maximize the forces we can achieve. For each resonance we also check the mode structure as explained below.

**2.4.1 Electrical impedance measurements.** To obtain an initial estimate of the strong resonances, we measure the electrical impedance while scanning the frequency of a transducer. Acoustic resonances within the device are identified as minima of the electrical impedance. To identify the resonances within the liquid-filled resonator, we look at the difference in the electrical impedance curve between the empty and the filled resonance chamber.<sup>27</sup> This technique works well for the top-transducer with its direct coupling into the sample volume. For the side-transducers on our chips, however, no significant difference in the electrical impedance measurement between the empty and the filled chamber can be seen due to the much weaker coupling of the resonator back to the piezo.

**2.4.2 Mapping by particle traces.** A straightforward way to identify working conditions with strong forces is to use a suspension of test particles. If we apply one of the candidate frequencies found as described above or simply scan the frequency and hit a resonance, then this is revealed by particles moving into a pattern defined by the mode structure. However, once particles have arrived at the equilibrium position, it can take them quite some time to disperse again, for example by Brownian motion or sedimentation, after stopping driving the transducers. This can be accelerated by switching to another force field configuration, for instance to a resonance with different mode structure, or by flushing in fresh suspension. However, both approaches can be rather cumbersome in practice to determining the full trapping landscape.

To overcome this issue, we propose a simple and convenient method by employing actively swimming micro-organisms as test particles.<sup>10</sup> They quickly disperse if not confined by acoustic forces. We prefer to use *Euglena gracilis*,



an easy to cultivate elongated protist with a typical length in of about 50  $\mu\text{m}$  (in its elongated form). Each acoustic resonance identified from the electrical impedance measurement can be easily but qualitatively compared with respect to levitation strength and resulting mode pattern. Switching on the top and one of the side-transducers, one can confine the specimens within the horizontal nodal planes into stripes. The frequency where the *Euglena* can be best restricted in their motion is a good indication where one can find the strongest resonance in the liquid. As the operator receives direct and immediate feedback, one can use this method to first find the strongest resonances and then to visualize the mode pattern at the desired driving frequencies.

We observe experimental patterns that are similar to the simulated ones, as illustrated in Fig. 5 which exemplifies the trapping landscape at a resonance near the 3rd harmonic of the x-transducer at 6.678 MHz (with the top-transducer also active). The results of the simulation and experimental data obtained from the trajectories of the swimming micro-organisms are shown back to back. Due to the imperfections of our machine-milled device, no exact quantitative comparison between experimental and simulation data can be made. Nevertheless, the pattern of this resonance reproduces some of the qualitative behaviour of our experimental findings quite well, such as the wavy horizontal trapping lines and the fact that the trapping lines become less defined towards the top and bottom margins of the chamber, where one is obviously also less successful in confining the swimming protists.

The visualization method we have used here is inspired by a popular approach in medical imaging to visualize structures of low intensity in a specific volume, called minimum intensity projection (MIP).<sup>35</sup> Here, a 2D image is generated from a 3D volume where each pixel displays the lowest attenuation value in the column of voxels along a chosen direction. In our case, the ‘third dimension’ is the time in the recorded movie. Analyzing every pixel in the top-view of background-subtracted movie recordings of *Euglena* swimming in the acoustic landscape and keeping just the

darkest (*most* attenuated) value in the time-line of the given pixel reveals local confinement: this type of ‘projection images’ shows where the specimens spend some time during the recording. Areas of relatively stronger and weaker confinement/forces can be mapped out, although not in a fully quantitative way. The procedure needs to be carried out for each identified resonance, but only once per assembly.

The micro-organism-based approach can be used to map out the strongest resonances in the chamber under 2D and 3D operation. In the result shown in Fig. 5 the transducers along x and z were active, and in Fig. 6a) the other side-transducer along y together with the z-transducer. With all three transducers active, the specimens are confined to a combination of islands and stripes, as shown in Fig. 6b). Due to the limited size of our sensor we cannot image the entire xy-cross-section of the chamber at once and the camera has to be rotated 90° to access the full propagation direction of each side-transducer.

## 2.5 Characterization of the acoustic force strength

The conversion of applied voltage on the transducers into acoustic forces cannot be done by a *global* calibration, since we have strong variations between different trapping sites. The user can get qualitative feedback on the relative strengths at a specific node by adjusting the voltages and qualitatively observing the effect on elongated particles. If, however, quantitative values of acoustic forces are needed, an on-site force calibration is required. This can, for instance, be accomplished in real time with the ‘Stokes drag method’, as detailed in ESI† S2. Using this method we have established the relative force per input voltage of the different transducers. Since the forces are inhomogeneous throughout the resonator and significantly differ between trapping sites, it is difficult to give a single number for the relative strength of the side-transducers (in terms of achievable force per input voltage). For the same driving voltage the x-transducer typically yields 6× stronger forces than the y-transducer, likely

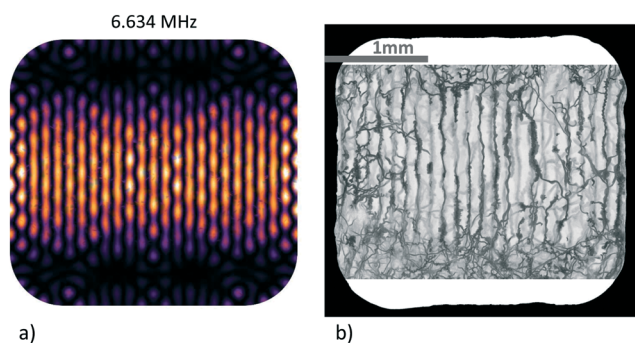


Fig. 5 Acoustic trapping landscape around the 3rd harmonic of the transducers (x- and z-transducers active): a) simulation, b) minimum intensity projection (MIP) visualization with trajectories of swimming microorganisms. The scale bar is shared between images.

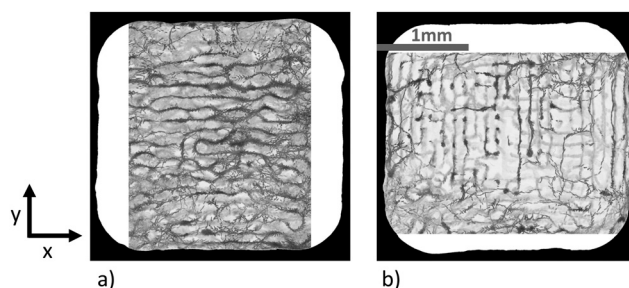


Fig. 6 Visualization of patterns in the resonator by means of micro-organisms: sub-images a) and b) are in the same chamber as shown in Fig. 5, filled with actively swimming *Euglena gracilis*, in a) the top-transducer (waves travelling along z) and the side-transducer along y are switched on, in b) all transducers are on (x, y, and z). The frequencies of the side-transducers are close to the 3rd harmonic frequency of the piezo. For the visualization every 10th frame of a movie recorded at 50 Hz was taken. The scale bar is shared between images.



since the resonances of the chamber and the piezo match better for the *x*-transducer. Due to its better coupling efficiency, the top-transducer is then again 6× stronger than the *x*-transducer.

Depending on the location inside the chamber, for a 10 μm polystyrene (PS) tracer bead and 10 V applied voltage, we found maximum forces in the range of several pN to tens of pN with the side-transducers, with the top-transducer we can achieve forces between tens of pN up to 100 pN. Please note that voltage refers to peak-to-peak voltage throughout the paper. Maximum pressure from side-transducers at 10 V ranges from 30 kPa to 200 kPa. For the top-transducer we have measured a range of 100 kPa to 300 kPa at 10 V for the 10 μm bead in different places. The trap stiffness at 10 V is 0.8 pN μm<sup>-1</sup> to 5 pN μm<sup>-1</sup> for top-transducer, 0.05 pN μm<sup>-1</sup> to 0.6 pN μm<sup>-1</sup> for side-transducers. Since the acoustic radiation force scales with particle volume, forces of several thousand pN are achievable for larger PS beads, *e.g.*, of 30 μm in diameter.

For long term monitoring of biological samples it is essential to estimate what kind of flow rates are compatible with these forces, for instance to ensure trapping of the particle while changing out the buffer-solution. As calculated from the maximal velocity displacement of a 30 μm bead, even for the weakest excitation direction the forces are at least on the order of 100 pN, and thus it would require only about 10 s to replace the solution, at a fluid flow speed of 400 μm s<sup>-1</sup>. Typically, the forces we operate with are even higher and a buffer-exchange can be done without affecting trapping.

### 3 Torques on trapped particles

We propose that in our device, two types of acoustically generated torque contributions play an important role: an angle-dependent torque, which reorients asymmetrically shaped particles, and a torque contribution mediated by viscous shear forces, which enables sustained rotation of a particle. The present section explains these contributions and summarizes some concepts which are essential in understanding the experimental results given in the next section.

Applying torque to an object by incident waves generally requires transfer of angular momentum. Optics and acoustics share some common aspects concerning linear and angular momentum flux.<sup>36,37</sup> The main differences between light and sound waves in this context are the consequences of acoustic pressure waves in fluids being longitudinal rather than transverse, as well as the direct mechanical influence of the liquid medium, *e.g.*, *via* acoustic streaming.<sup>38–40</sup>

This work mainly focuses on acoustic waves to induce torques, but let us, nevertheless, start by stating some facts from optical micro-manipulation as a starting point to understand the commonalities and differences to acoustic wave torque. In optics, rotations can be induced by the absorption or scattering of light, transferring angular

momentum encoded on the polarization of the beam (spin) or the phase gradient (orbital angular momentum).<sup>41,42</sup> Absorption of photons carrying angular momentum induces a rotation of the object. In some situations, however, absorption may be an impractical way to rotate an object, since it also leads to heating. A non-zero torque can also result if an asymmetry in the scattering is present, *e.g.*, for particles of asymmetric shape or anisotropic material.<sup>43,44</sup> And chiral particles may even experience a torque in optical fields which have no angular momentum.<sup>45</sup>

Non-zero time-averaged torques on an object mediated by acoustic fields have been studied for many years since the 1950s,<sup>46–49</sup> theoretically as well as in view of lab-on-a-chip applications. The components of an acoustically generated torque follow the general scaling rule,<sup>36,50</sup>

$$T = \tau_0 Q \text{ with } \tau_0 = VE_0, \quad (2)$$

where *V* denotes the volume of the particle and *E*<sub>0</sub> stands for the acoustic energy density, which depends on the pressure amplitude *p* of the incoming wave, the density *ρ*<sub>0</sub>, and the speed of sound *c*<sub>0</sub> of the liquid medium, *E*<sub>0</sub> = *β*<sub>0</sub>*p*<sup>2</sup> (with *β*<sub>0</sub> = 1/2*ρ*<sub>0</sub>*c*<sub>0</sub><sup>2</sup>). *τ*<sub>0</sub>, the product of the particle volume and the incoming intensity, is weighted by a dimensionless parameter *Q* of the order of unity, which contains the essential information on the transfer of angular momentum to the particle, either by absorption<sup>51</sup> or by scattering.<sup>48‡</sup> *Q* depends on the symmetry of the particle, the angular momentum content of the incident acoustic field(s), and on the acoustic contrast (*i.e.*, on the difference in density and compressibility of the particle compared to the surrounding fluid). It can be calculated from scattering theory. For non-absorbing fluids (and particles) a non-zero *Q* requires some asymmetry in the scattering by the particle, this means that a sphere in a *frictionless* fluid experiences no torque.

#### 3.1 Acoustic radiation torque

The contribution known as *acoustic radiation torque*<sup>46–50</sup> depends on the relative orientation of the particle and the incident wave(s). It can be depicted as the torque arising due to the acoustic radiation forces<sup>52</sup> on individual parts of an extended, asymmetric particle. As such it prevails in *inviscid* fluids (*i.e.*, kinematic viscosity *η* = 0).

As an example, a small spheroidal particle orients itself such that the shortest axis will align with the direction of strongest confinement (trap stiffness). An oblate spheroid in a plane standing wave will behave as if squeezed in by the acoustic force field into the nodal plane. For small particles of spheroidal shape (with long axis *a* and small axis *b*) one can derive an explicit expression for the acoustic radiation torque.<sup>50</sup> Such a particle will experience a maximal torque when oriented at 45° to a plane wave, but no torque when

‡ Please note that here *T* refers to a non-zero component of the torque in some specific direction, the full angular dependence of the torque vector in 3D is not addressed at the moment.





placed at an angle of  $0^\circ$  as well as  $90^\circ$ . When the object shape approaches a sphere the torque is found to vanish. Due to the typically strong viscous damping of the motion of small particles in a fluid, a particle will usually approach a stable equilibrium position and orientation without oscillations. Thus, the acoustic radiation torque provides us with a tool for alignment or reorientation of non-spherical particles.

### 3.2 Viscous torque

Close to the surface of a rigid particle, the relative vibrational motion of the fluid due to an acoustic wave has to cease to adhere to the no-slip condition. This induces viscous shear forces in the boundary layer that act both on the fluid and on the particle. As a result, one can observe acoustic streaming in the fluid and an *acoustic viscous torque* acting on the particle. In contrast to acoustic radiation torque, viscous torque can also occur for spherical or cylindrical objects. In such a case the acoustic field itself has to carry some angular momentum to induce a torque, which can be created, *e.g.*, by using two orthogonal standing waves of equal frequency with a  $90^\circ$  phase shift. Wang *et al.* in 1977 (ref. 53) used such a configuration in one of the first experiments to induce rotation of a cylinder by acoustic waves in air. The viscous torques also gives one the means to very effectively spin Poly(methyl methacrylate) (PMMA) spheres of some  $100\ \mu\text{m}$  in water with a steady-state rotational speed determined by the balance of the acoustic torque and the frictional drag torque.<sup>54</sup> Smaller particles are found to spin faster and reach equilibrium more quickly. These effects are well understood and numerical simulations and experimental results are in excellent agreement.<sup>55,56</sup>

To describe the viscous torque in such a situation in the framework of eqn (2),

$$T_{\text{visc}} = V \frac{\delta}{a} 2p_x p_y \beta_0, \quad (3)$$

one has to add an imaginary term proportional to  $\delta/a$  to the (usually dominant) dipole scattering amplitude,<sup>57,58</sup> with  $a$  the characteristic particle size and  $\delta$  the thickness of the viscous boundary layer  $\delta = \sqrt{2\nu/\omega}$  depending on the kinematic viscosity of the fluid  $\nu = \eta/\rho$  and on the angular frequency of the exciting acoustic frequency  $\omega$ . For 1 MHz to 10 MHz in water  $\delta$  has values from  $0.53\ \mu\text{m}$  to  $0.17\ \mu\text{m}$ . Furthermore, the viscous torque is proportional to the 'mixed' term  $\propto 2p_x p_y$  of the sound pressure in the coherent superposition of the two orthogonal out-of-phase standing waves, which is the term containing angular momentum.

### 3.3 Multi-mode excitation and angular momentum

Since the angular momentum in the acoustic field plays an essential role for viscous torques, let us briefly discuss the distribution of acoustic angular momentum in a resonator which resembles the one used in our experiments (in sec. 4). As an example we use the (horizontal) modes introduced in sec. 2.3.2 to explain how phase vortices may arise at pressure

nodes, which means that non-zero angular momentum locally occurs around some trapping spots. For clarity, we look at the resonances of the fundamental of our transducers near 2 MHz, but similar features are also present for the 3rd harmonic (around 6 MHz), but would be harder to discern in the graphics due to their finer scale. Driving two eigenmodes of the resonator at frequencies  $f_1$  and  $f_2$  with a single frequency  $f$  leads to a coherent superposition of the two mode functions. Assuming Lorentzian line-shapes of the modes, the coefficients of the superposition are  $\sim [1 + i(f - f_k)/b_r]^{-1}$ , with  $k = 1, 2$ .  $b_r$  denotes the width of the resonances. It is always possible to choose  $f$  somewhere in the interval between the two eigen frequencies such that a relative phase-shift between the two complex coefficients of  $90^\circ$  results, provided that the spacing  $f_2 - f_1$  (of excitable resonances) is larger than  $2b_r$ .

In Fig. 7a) the superposition of two orthogonal stripe patterns with eigenfrequencies  $f_1 = 2.237\ \text{MHz}$  and  $f_2 = 2.404\ \text{MHz}$  is chosen as an example, which comes close to the idealized situation of orthogonal plane waves. For the modal width we have assumed  $b = 80\ \text{kHz}$  (HWHM) which lies in the range of the actual values in our chambers. The small images at the top display the intensity maps of the two eigenmodes and their superposition, and in the phase map below only low-pressure regions are plotted (values above a chosen threshold at 40% of the amplitude are left white) and trapping spots (zero pressure sites) are marked by black dots. The phase map of the pressure field demonstrates the existence of several pressure nodes with phase vortices.

However, realizing such a pure situation in practice requires particular care, *e.g.*, a square chamber with two orthogonal transducers operating at the same frequency.<sup>56</sup> Nevertheless, in our simulations we have seen that the occurrence of dark spots with local angular momentum is generic in our type of resonator. As described in sec. 2.3.2, the rounded edges lead to a coupling between the horizontal directions, *i.e.*, any eigenmode contains contributions from plane acoustic waves travelling in orthogonal directions. Similar phase structures, as shown in Fig. 7b), also occur in the superposition of the first eigenmode (with pronounced stripes) with its *adjacent* eigenmode, but the vortex structures are less symmetric. Inevitably this nearby mode is also excited to some extent when addressing the first mode due to the finite resonance width and the small spacing of 28 kHz.

## 4 Particle rotation induced by acoustics and optics

From the brief summary on the origin and the effect of acoustic torques given in the previous section, we conclude that we can induce two different types of particle rotations in our device: in sec. 4.1, we will show how an asymmetric particle *transiently* rotates to change its orientation in response to a change in the acoustic field, reaching a new equilibrium position. The other case of *sustained* rotation of





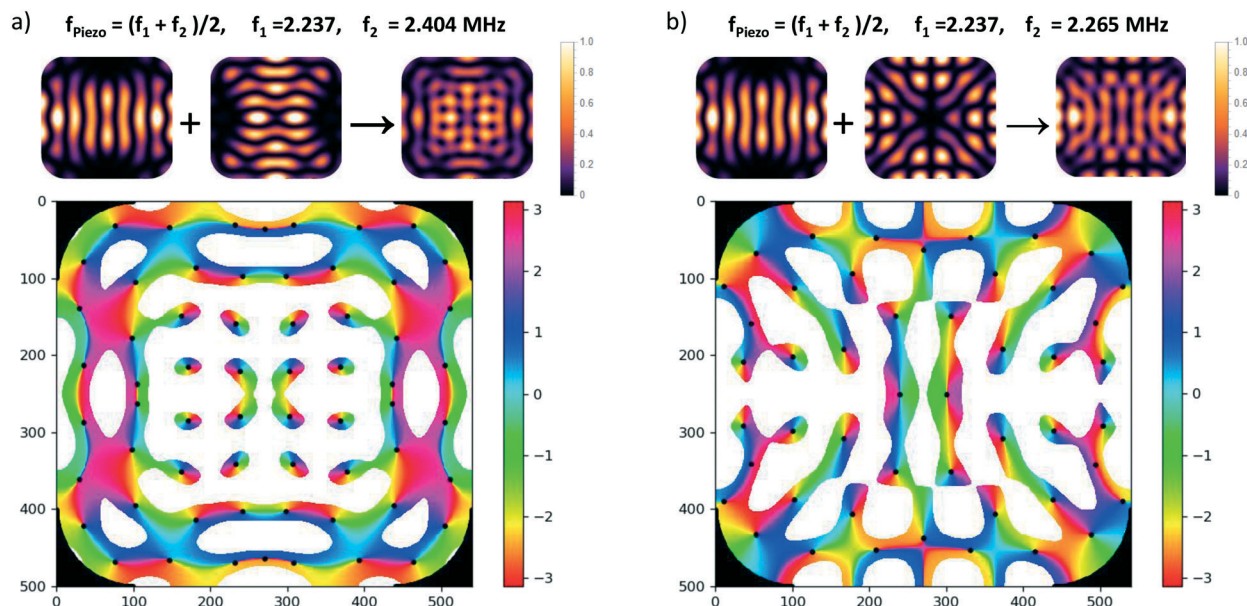


**Fig. 7** Angular momentum carrying superpositions of resonator modes: the small images on the top show the intensity of the pressure patterns of the eigenmodes which are coherently superposed with a relative phase close to  $90^\circ$  by choosing the values given at the top. The color graph below depicts the phase of the superposition field in the interval  $[-\pi, \pi]$ . Only low-pressure regions are plotted (values above a chosen threshold are left white) and trapping spots (zero pressure sites) are marked by a black dot. a) Superposition of orthogonal stripe patterns, b) superposition of two adjacent eigenmodes. Such superpositions can be created by exciting two overlapping resonances by a transducer with driving frequency between the two resonance frequencies  $f_1$  and  $f_2$ .

the particle in a viscous fluid (such as biological samples in water) in *static* acoustic fields will be treated in sec. 4.2, including the option to facilitate rotations by additionally using optical fields demonstrated in sec. 4.3.

#### 4.1 Controlled reorientation of asymmetric particles under the influence of the acoustic radiation torque

Reorientation by the acoustic radiation torque provides a useful means to inspect a specimen from an altered angle. This is particularly useful for large biological specimens. Since they are very rarely perfectly symmetric, but typically possess some irregular shape, this is a generally applicable method. If subjected to acoustic forces, the samples not only move to trapping sites (typically to pressure nodes), but also reorient themselves under the influence of the acoustic radiation torque. This is analogous to optical forces aligning an elongated particle trapped by optical tweezers along the optical axis.

Repeatedly changing the orientation of the particles by acoustic radiation torque requires some modulation of the incident field(s). In the literature, different methods have been investigated to rotate elongated particles, short glass fibers, or polymer particle clusters, either in a step-wise way by changing the propagation direction of the ultrasound as a function of time or in a continuous way by sweeping its amplitude, frequency or phase.<sup>49,59,60</sup>

A particle of roughly elliptical shape will settle into an orientation where its shortest axis aligns with the direction of steepest trap stiffness at the trapping spot.

This minimizes the potential energy of the object in the acoustic trapping potential. In our device, we can adjust the orientation of the particle in a controlled way by changing the driving voltages of the three transducers. When the top-transducer is strongest, we find that oblate particles (of relatively uniform acoustic contrast-factor distribution) align flatly within the horizontal trapping nodes, with their shortest axis being vertical, which amounts to maximal cross-section of the particle with the nodal xy-plane.

At low voltages of the side-transducers, the particle's location is confined, but the orientation of the particle *within* the nodal plane is not strongly locked in. Raising the voltage of one side-transducer reorients the particle's largest axis in a controlled manner along the axis with the weakest confinement, while the vertical position of its shortest axis is still maintained by the (still dominant) top-transducer. When one of the side-transducers becomes the strongest, the particle's shortest axis is now aligned with the corresponding trapping direction, the *x* direction for the *x*-transducer, and the *y*-direction for *y*-transducer. This is demonstrated in Fig. 8 with a 45  $\mu\text{m}$  long oblate starch particle. The particle is trapped with three active transducers around 6 MHz, and by increasing the voltage of one of the transducers at a time, the orientation of the particle can be controlled. The top-transducer at 6.844 MHz with frequency modulation at 50 kHz is kept at 3 V, while *x*- and *y*-transducers at 6.678 MHz and 6.807 MHz, respectively, are set within a range of 1.4 V to 5.2 V and 6.8 V to 17.6 V (low to high voltage).



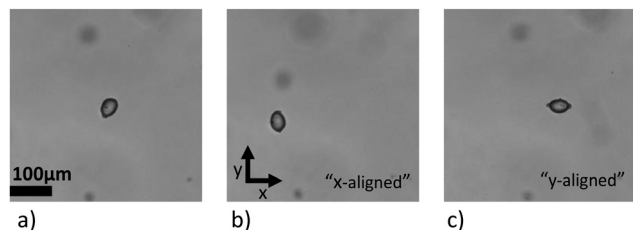


**Fig. 8** Reorientation of a starch grain: by tuning the relative strengths of the three active transducers, the orientation of an elongated oblate particle can be controlled. In a series of wide-field images taken with the imaging axis along  $z$ , one can see in a) that the top-transducer is strongest and the particle is oriented with its largest cross-section settled into a top-transducer node in the  $xy$ -plane. When the voltage of either the  $x$ - or the  $y$ -transducer is increased to make it dominant, shown in b) and c), the particle's major axis aligns to the nodes of the  $x$ -transducer or the  $y$ -transducer, respectively.

## 4.2 Sustained rotation in stationary acoustic fields

To induce *sustained* rotation of an object in the liquid (which damps the motion), without any temporal tuning or modulation of the acoustic fields, requires continuous transfer of angular momentum from the impinging waves to the particle over time.<sup>36</sup> As explained in sec. 3, viscous torque provides such a mechanism to induce sustained rotation. In this section we show that this approach is applicable for a variety of particles, in particular for large living specimens.

In practice both, acoustic radiation torque and viscous torque, are present simultaneously. The actual behaviour observed in an experiment is governed by an interplay between these mechanisms and other contributions, leading to a complex and diverse behaviour. We present examples that demonstrate strategies for inducing rotation in a controlled manner by a combined action.

**4.2.1 General observations.** In our resonators we have successfully induced sustained rotations along reproducible trajectories in stationary acoustic fields for a wide variety of relatively large (40–200  $\mu\text{m}$  diameter) specimens held in a fixed trapping position. This includes cells, pollen and starch grains, micro-organisms, as well as chains and clusters thereof.

Fig. 9 shows a selection, with examples of increasing complexity. Fig. 9a) shows a rotating single, relatively small pollen grain from *Tragopogon pratensis*, 9b) a larger one from *Sansevieria trifasciata*. c) Shows a cluster of starch grains of various sizes, some actively rotating, some not. Finally, in d) we see a cancer spheroid performing a sustained rotation.

From this we gather that sustained rotational behaviour is commonly observed. However, we find that the behaviour depends on several parameters, not all of which are sufficiently well known in a given experimental setting. The shape of the particle, as well as their inner structure, affect the acoustic forces and torques. Particles with roughly spherical shape are more likely to show sustained rotation. Also the local field at the trapping site plays an important role. We often observe different behaviour of similar objects

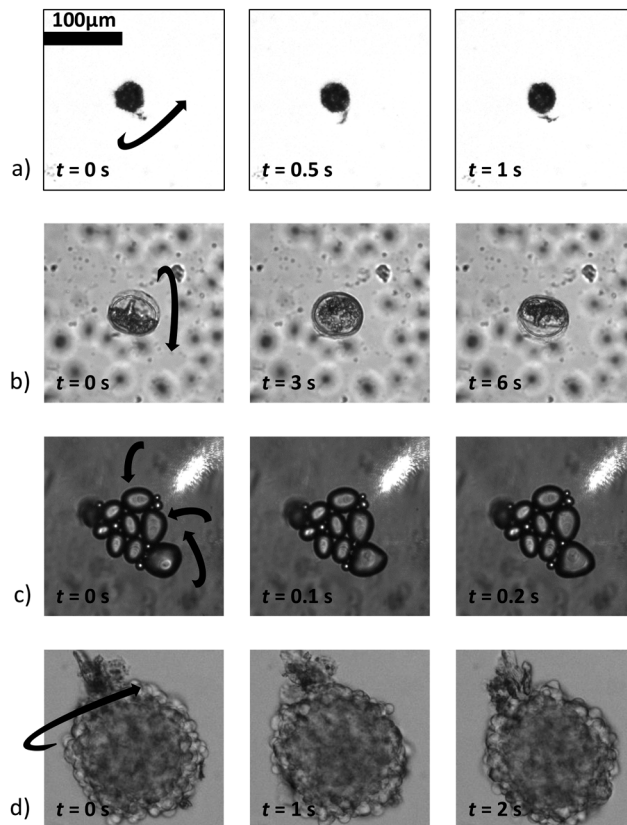


**Fig. 9** A wide variety of individual and clustered samples (ranging from 35  $\mu\text{m}$  to 170  $\mu\text{m}$  in length) performing a sustained rotation in the acoustic traps around an axis orthogonal to the imaging axis. One pollen grain from a) *Tragopogon pratensis* and b) *Sansevieria trifasciata*. In panel c) a potato starch cluster of which several connected grains are rotating. d) Shows a cancer cell spheroid. The scale bar is shared between images (ESI† Movies S2–S5).

in neighboring trapping sites. This is due to the intricate force landscape in our resonator, as presented in sec. 2.3 and Fig. 7. Furthermore, the local field can be significantly altered by particles nearby due to secondary acoustic radiation forces (Bjerknes forces). In particular, air bubbles, which strongly scatter the acoustic field, show a strong effect. Let us remark here that planar arrays of localized micro-bubbles which oscillate under acoustic excitation are an alternative way to induce controlled rotation<sup>61</sup> of several single cells, but samples with gas-filled cavities and bubbles behave quite differently compared to solid micro-objects<sup>62</sup> and will not be treated here.

**4.2.2 Strategies to induce sustained rotation.** The general facts explained in sec. 3 pave the way for a procedure to evoke sustained rotation that works in the majority of practical applications. In view of tomographic reconstructions of volumetric data (attenuation and refractive index distribution) planned for the future, we are especially interested in sustained rotations around an axis that lies within the horizontal plane, orthogonal to the imaging direction, which provides new information about the particle's structure.



We always see the combined effects of acoustic radiation torque, acoustic viscous torque, and possibly additional torque due to acoustic bulk streaming around the particle, all acting together. As described in sec. 3.1 the acoustic radiation torque acting on its own ‘locks’ an asymmetric particle into a certain orientation. An approximately spheroidal particle with axes lengths  $a < b < c$  is aligned such that the shortest axis  $a$  points into the direction with strongest confinement, whereas the longest axis aligns along the weakest confinement. To induce sustained rotation, the largely orientation-independent viscous torque needs to overcome the (maximum) acoustic radiation torque. This can be achieved by tuning the strength of the individual transducers (operating at different frequencies) such that the confinement strength (trap stiffness) is the same in each direction. Close to the trapping site this yields an isotropic trapping potential, where the total acoustic radiation torque vanishes also for an asymmetric particle.

For large particles it is more challenging to reach this condition. One reason is the different scaling properties of the torque contributions, according to eqn (2) and (3). The peak contribution of the acoustic radiation torque (*i.e.*, the peak value for a specific orientation) scales as  $V \sim a^3$ , whereas the viscous contribution of the torque as  $\sim V\delta/a \sim a^2\delta$ . With  $\delta < 1 \mu\text{m}$ ,  $\delta/a$  is small at driving frequencies of a few MHz, which means that the acoustic radiation torque grows faster with particle size than the viscous torque (given the same acoustophoretic contrast and shape asymmetry). Therefore, for large asymmetric particles the acoustic radiation torque is usually the dominant contribution, but leads only to transient motion, tilting the particle into a certain angular orientation rather than sustained rotation. Furthermore, large particles experience more of the trapping landscape away from the trapping site, where it may become anisotropic.

**4.2.3 Relative strength of acoustic radiation torque and viscous torque.** To get information about the (relative) strength of the angle-dependent acoustic radiation torque and the approximately constant viscous torque, we analyze the rotational motion of a particle showing sustained rotation. In the steady state, the rotation rate is determined by a balance between the total acoustically generated torque and the opposing Stokes drag torque. The combined influence of angle-dependent acoustic radiation torque and constant viscous torque leads to non-uniform rotation of the particle: at some orientation-angles of the object the two types of torques are acting together, and at others they are opposing each other. The motion may also appear somewhat ‘wobbly’, but with the rotation axis still sufficiently well oriented.

Movies of spinning particles, such as the spheroidal starch grain of Fig. 10, may be used to investigate the relative portion of ‘accelerating’ and ‘decelerating’ parts in the rotational motion. In the ESI† Movie S6 one can see that the grain spends quite a long time in one orientation and the quickly rotates around to the opposite side, which is a clear

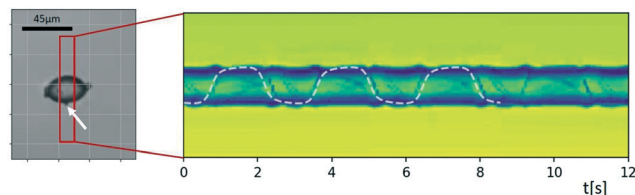


**Fig. 10** Sinogram of an ellipsoidal starch grain rotating with a strongly inhomogeneous rotation velocity. The acoustic radiation torque, which is angle-dependent as it depends on the object's orientation, is accelerating and decelerating the rotation around the long axis induced by the viscous torque. Tracking the small feature attached to the surface (marked by a white arrow) and fitting its trajectory to a curve resulting from a constant and an angle-dependent rotation rate allows one to estimate the ratio of the two torques. In the ESI† Movie S6 one can see that the grain spends quite a long time in one orientation, which is followed by a quick revolution around the opposite side, since the two torques in this example are of similar strength (with the acoustic radiation torque amounting to  $\sim 75\%$  of the viscous torque).

indication of the existence of an angle-dependent contribution to the torque.

The sinogram in Fig. 10 was created by applying MIP inside the red rectangle. Tracking the small feature attached to the surface (marked by a white arrow) and fitting the resulting trajectory to a rotation containing a constant and an angle-dependent angular velocity allows one to derive an estimate of the relative strength of acoustic viscous and radiation torque. Assuming that the orientation angle  $\phi(t)$  for rotation of the particle about its long axis follows the differential equation  $\phi(t) = \Omega_1 + \Omega_2 \sin[2\phi(t) + \phi_0]$ , the projected position of the marked feature as a function of time  $t$  is proportional to  $\sin\phi(t)$ , found by integrating the differential equation. Here we use the model that the viscous torque is described by an angle-independent contribution  $\Omega_1$ , and the acoustic radiation torque depends on the orientation-angle with a peak value of  $\Omega_2$  of periodicity  $\pi$ . The best fit of this model, which is shown as a dashed line in Fig. 10, gave us the result that in the present case the two torque contributions are of similar strength, with the acoustic radiation torque amounting to  $\sim 75\%$  of the viscous torque. Rough estimates based on eqn (2) and (3) are consistent with this.

**4.2.4 Control of rotation by side-transducer strength.** We study the dependence of the rotational motion on the side-transducer voltage in more detail in the next example featuring a pollen grain from a *Hibiscus* flower of size  $115 \mu\text{m} \times 120 \mu\text{m} \times 126 \mu\text{m}$ . In this experiment the transducers were operated at the frequencies stated in sec. 4.1.

Fig. 11 shows the onset/stopping of rotation and changes of the axis of rotations and the rotation rate  $1/T$  as a function of increasing and then again decreasing driving strength of the  $x$ -transducer. Initially, the top-transducer creates the strongest field, the  $x$ -transducer is on low voltage, the  $y$ -transducer off, and the pollen aligns ‘flatly’ with the horizontal nodal plane of the strong  $z$ -transducer, with its shortest axis locked-in vertically by the top-transducer, as expected from above considerations (we remark that in the current example the top-transducer alone also induces some





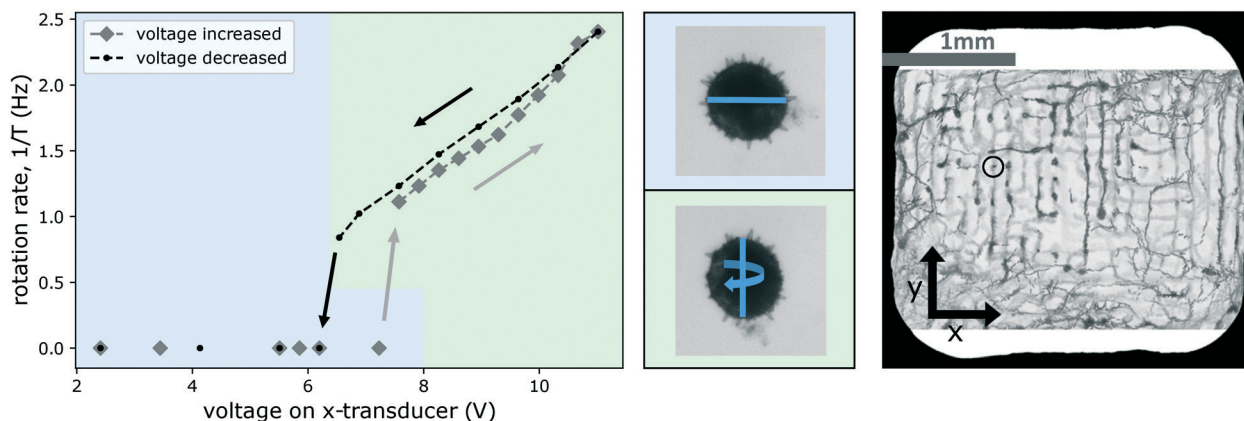


**Fig. 11** Changing the rotation axis and rotation rate of a *Hibiscus* pollen grain (trapped at the site indicated in the image on the right) by tuning the strength of one of the transverse transducers. The graph shows that increasing the voltage (diamond-shaped data points in gray) beyond about 7 V there is a threshold for the onset of rotation. Beyond this threshold the alignment of the rotating particle is also different, as shown in the middle row with the blue line indicating the major axis of the grain which is 126  $\mu\text{m}$  long. For a better visualization of the two different orientations of the particle, in the diagram we use green and blue background color-coding. On the way 'down', reducing the voltage again (circular data points in black), rotation is seen to persist down to a slightly lower voltage (ESI<sup>†</sup> Movie S7 shows the particle rotating at 1 Hz and at 2.4 Hz).

confinement along the  $y$ -direction, as a result the initial orientation of the particle is as if under the influence of the  $y$ -transducer, although it is not switched on).

When the voltage of the  $x$ -transducer is increased, first no motion occurs, until a certain threshold (just above 7 V) is reached, where the particle spontaneously readjusts, aligning itself according to the potential created by a now stronger  $x$ -transducer. This change of orientation is visible as a change in apparent cross-section of the pollen. In Fig. 11 we highlight this by color-coding, with a blue background indicating the alignment under the influence of a dominating top-transducer, and a green one indicating alignment under the influence of the  $x$ -transducer (particle alignment corresponding to the graph is shown in the middle row in Fig. 11). The forces generated by the top-transducer in this experiment lie in a range of 10 pN to 60 pN, and comparable forces can only be reached by the  $x$ -transducer at the highest investigated powers (reaching 8 pN to 26 pN).

Beyond this threshold, the particle starts to rotate around an axis parallel to the  $y$ -axis, as shown in the graph, rotating between alignment of the two largest cross-sections to either top- or  $x$ -transducer nodes. Increasing the voltage further (along the gray diamond markers in the curve) in steps, results in faster rotation. Eqn (2) predicts a quadratic dependence of the torque on the pressure  $p$ —which we have verified for single transducer operation—but the dependence is more complicated when two transducers are used. Similar to the experiment of Fig. 10, the rotation velocity is not constant, and the particle spends more time with its largest cross-section aligned to the top-transducer nodes. The time in this alignment decreases for larger voltages of the  $x$ -transducer.

Decreasing the driving voltage again (along the black line) results in a slightly shifted curve for the rotation rate. On the

way down, the pollen stays somewhat longer in the  $x$ -transducer alignment (until  $\sim 6.5$  V is reached). This delay in settling into the new stable orientation is common in systems with friction: one cannot predict exactly when the flipping into the new equilibrium position is going to take place, it depends on the exact nature of the stochastic micro-environment around the particle. The rotation stops after the reorientation has happened. We often observe small differences in the characteristics of the rotations (onset/stopping, direction of rotation axis) when repeatedly increasing and decreasing the voltages, as some small changes may take place (e.g., a slight translation of the trapped particle or of an air-bubble or particle somewhere), which make it difficult to maintain the exact same operating point (particle location and orientation).

Carrying out the same experiment as shown in Fig. 11 in the other direction (tuning the  $y$ -transducer) did not lead to the same kind of readily interpretable results. The influence of the  $y$ -transducer seemed to be masked by other effects that were superposed. The overall behaviour was not as stable, and often ended in a rotation around the  $z$ -axis for large driving voltage. This asymmetry in behaviour is probably caused by the fact that the frequency spacing between the two transducers ( $z$  and  $y$ ) was smaller than in the first case ( $z$  and  $x$ ), changing from a difference of  $\sim 170$  kHz to one of  $\sim 40$  kHz, giving rise to crosstalk effects which affected the trapping pattern in 3D. Additionally, since we do not have a  $xy$ -symmetric chamber, the situation may be less favourable for inducing a controlled rotation when exciting from the other direction around the given frequency. The bulk streaming excited in the chamber also seemed to affect the particle's motion. The MIP visualization technique introduced in sec. 2.4 provides a useful means to directly demonstrate the presence of streaming in the (wider) periphery of the trapped pollen. In Fig. 12, traces from debris



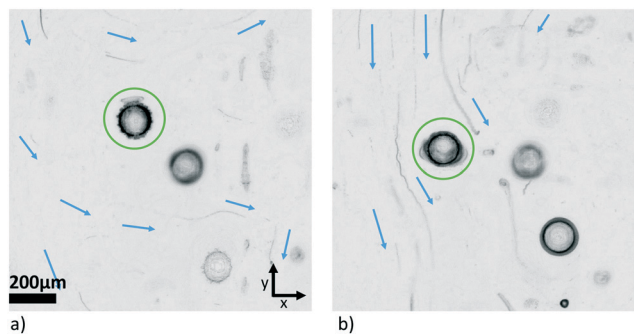


**Fig. 12** Minimum intensity projection to visualize the streaming patterns with dominating side-transducer propagating along a) x-axis, and b) y-axis, respectively. The pollen grain of interest is marked by a green circle.

in the liquid show that streaming is taking place. Locally around the particle it largely takes its direction from the direction of propagation of the field emanating from the side-transducers, *i.e.*,  $x$  in a) and  $y$  in b), but in the region around the examined object the streaming was observed to be more complicated in situation b) than in a).

Let us finally remark our observation that for even larger samples than the *Hibiscus* pollen, when the diameter exceeds the acoustic wavelength (*e.g.*, 250  $\mu\text{m}$  for 6 MHz) a problem occurs: such samples are practically fixated, because they are sufficiently large to be firmly ‘locked-in’ into *two* trapping spots along the  $z$ -direction, which makes it difficult or even impossible to induce continuous rotation in the described way.

### 4.3 Optical manipulation of acoustically trapped particles

Purely optical traps have already been utilized to rotate or reorient cells for tomographic phase microscopy,<sup>63–65</sup> and optical trapping beams have been engineered based on the measured 3D refractive index map of samples retrieved from optical tomography.<sup>66,67</sup> In our device, optical tweezers are used in an auxiliary way, since purely optical forces are too weak to levitate heavy samples such as the ones investigated in this work,<sup>12</sup> but can be strong enough to induce an additional bias-force for translating particles or redistributing them between acoustic pressure nodes, as we have done in the past.<sup>68</sup> Although in the majority of cases we have been able to successfully induce rotation by trying out various acoustic field configurations, we have nevertheless found it very useful to have an additional ‘handle’ to turn, especially one with the excellent dynamic control and fine spatial scale provided by HOT.

The optical trap in the form of one or more laser spots can be dynamically steered around the acoustically levitated particle in a highly controlled way. If we target a (vertical) laser beam at the edge of an acoustically levitated particle, we expect the vertical component of the optical force to rotate the particle. The horizontal component will lead to a translation (typically towards the beam). To induce a

continuous rotation, the radiation pressure must be kept off-centered on the particle. Thus balancing the horizontal optical force component to fix the particle position is advantageous, which can be done both with additional optical traps or with horizontal acoustic confinement. In the case of additional optical traps, for example two traps would be used to hold the particle on a symmetry axis, and a third would be placed off-axis to form a triangular shape of the traps and induce the rotation. Alternatively, the particles horizontal position (in addition to its vertical) is fixed by acoustics and we only need one optical trap to induce a rotation.

Indeed, we observe such a behaviour, as shown in Fig. 13. In this example we used a cancer spheroid. Cancer spheroids are used in Oncology to study the development of various cancer types and to screen the effect of therapeutic measures on the cellular level, in the present case the type used to study the oncogenesis of neuroblastoma at the Medical University of Innsbruck.<sup>69,70</sup> Pointing a laser beam (marked by a red circle in Fig. 13) at the edge of the acoustically confined spheroid, induces a continuous rotation, which does not occur with acoustic trapping alone. This allows us to induce rotation for rather large specimens, for which it is more challenging to succeed with acoustics alone. Please note that the laser spot appears larger than its actual size in the images due to residual reflections. Typically the optically triggered rotation immediately stops when the tweezers are no longer overlapping with the sample. This indicates that the rotation is mainly induced by the optical radiation pressure, and the position of the tweezers on the sample determines the particle's orientation and rotation.

When performing these particle manipulation experiments, where we want to manipulate a particle confined to a horizontal nodal plane by the top-transducer, we have observed an additional effect: placing laser beams, *e.g.*, at the edge of a spruce (*Picea abies*) pollen grain induces a rotation and also a streaming of the fluid, as shown in Fig. 14. Here, the laser was split into three traps (marked by red circles) to use two of the spots to hold the particle and a third to rotate (traps in triangular shape). However, the horizontal acoustic force was sufficient to fix the position of the particle, and the three traps are in principle used as one trap in the examples included. To visualize the streaming in

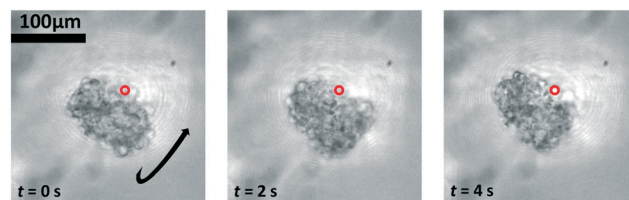


**Fig. 13** Combined optical/acoustic rotation of spheroid: the spheroid did not rotate under acoustic trapping alone. By placing the HOT (marked by a red circle) on the spheroid, one can change its orientation. With the HOT placed at a specific location on the edge of the spheroid, a continuous rotation could be induced (ESI† Movie S8).



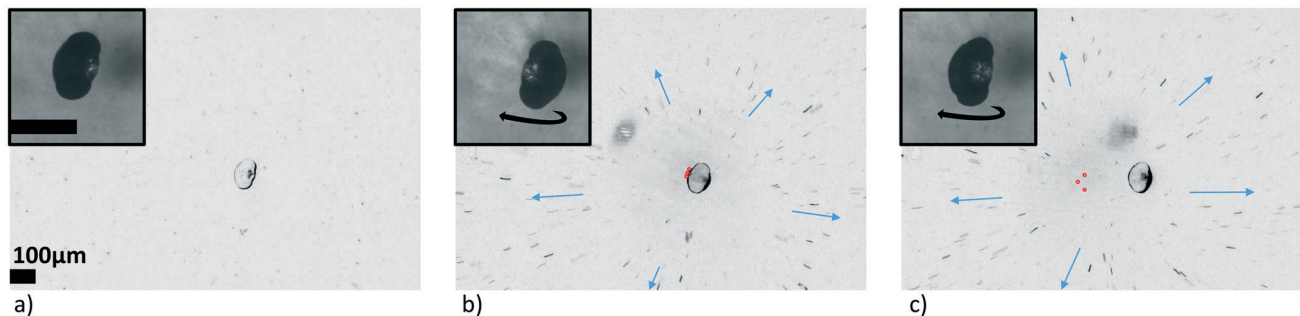


**Fig. 14** Optically induced acoustic streaming: a) an acoustically trapped pollen grain from *Picea abies* is almost stationary under the given acoustic trapping parameters (ESI† Movie S9, ‘HOT off’). b) Placing the HOT (three spots marked by red circles) at the edge of the sample induced a continuous rotation of the sample (ESI† Movie S9, ‘HOT on’). c) The continuous rotation prevailed when the trap was moved far away from the sample (ESI† Movie S10). An identical treatment (minimum intensity projections of 220 frames) was applied to each of the three movie segments, revealing that outward streaming from the HOT center is present in b) and c), but not in a).

a single image, we apply the minimum intensity projection along the time axis, as described in sec. 2.4.2, to show the traces of small test particles. Both rotation and streaming are absent without the laser, see Fig. 14a). The streaming persists independent of whether we point the laser at the particle or at some distance away from the particle. As apparent in Fig. 14c), the streaming within the observation plane points out radially from the laser beam position. Interestingly the rotation also persists.

In this case apparently the induced fluid flow leads to the sustained rotation of the particle *via* viscous drag, at least indirectly: it could be that the drag torque in combination with the acoustic viscous torque overcomes the acoustic radiation torque acting to lock the particle in a fixed orientation. This effect of inducing a particle rotation by a flow is similar to what happens in ‘thermo-optical tweezers’,<sup>71</sup> which utilize the convective flow induced by heating the fluid by light absorption at gold-coated cover slips to rotate the single cells around a transverse axis. However, in our case, the flow is not induced by convection due to laser heating, because it is strongly reduced if we keep the laser on but switch off the acoustic field. Nevertheless we suppose that a local temperature rise due to light absorption in the fluid plays a significant role. If we exchange the fluid by heavy water, which exhibits a smaller absorption of the near-infrared laser light, we observe a significant reduction in the optically induced streaming. We believe that the local temperature rise leads to a local modification of the fluid properties, *e.g.*, viscosity, that triggers an enhanced acoustic streaming, similar to what happens at a surface. The exact mechanism is yet unexplored and further quantitative investigations are needed.

## 5 Conclusions

We have presented a new type of sono-optical device based on a microfluidic chip, as an easy-to-use approach for handling and studying biological samples of a few hundred  $\mu\text{m}$  in size in liquid suspension. In particular, it can be used to induce controlled rotation around an axis that can be

chosen, which is an essential requirement for the 3D inspection of the sample, *e.g.*, for volumetric imaging or optical tomography.

Specifically, we have demonstrated the effectiveness of a strategy for aligning or spinning biological samples in a controlled way: by tuning the relative strengths of the transducers (a strong optically transparent top-transducer for levitation and two weaker side-transducers, all operating at MHz frequencies) one can affect the relative strength of the orientation-angle dependent acoustic radiation torque  $T_{\text{rad}}$  arising from pressure gradients and the acoustic viscous torque  $T_{\text{visc}}$  arising from the shear forces at the viscous boundary layer of the particle. The former locks an asymmetric object into an orientation corresponding to lowest potential energy in the acoustic potential. One can determine the orientation direction the particle will settle into by tailoring the potential in 3D *via* the resonance modes excited by the active transducers.

For continuous rotation of the over-damped particle in the liquid, the acoustic viscous torque  $T_{\text{visc}}$  has to overcome the acoustic radiation torque  $T_{\text{rad}}$ . We found that one can facilitate rotation by choosing appropriate relative strengths of top- and side-transducer(s) to create a largely isotropic potential around the trapping location of the particle, since this reduces  $T_{\text{rad}}$ . The viscous torque  $T_{\text{visc}}$  driving the continuous rotation of the particle is created by the uptake of angular momentum by the viscous liquid around the particle. Our simulations have revealed the optimal conditions for creating angular-momentum carrying trapping nodes when exciting neighboring resonances of overlapping widths. This kind of optimization, however, requires detailed information of the 3D mode patterns in the resonators, which is often not directly available. In order to get at least a qualitative impression of the trapping nodes and of the streaming in the resonance chamber, we have developed some practical techniques utilizing suspensions of swimming micro-organism and visualizing their traces in an approach inspired by the ‘minimum intensity projection’ in medical imaging. Moreover, we have shown that – whenever the condition that the viscous torque exceeds the acoustic radiation torque is





not (easily) achievable, for instance for larger and/or more asymmetric particles – auxiliary optical tweezers are suitable for inducing rotation, either by direct optical radiation effects or by optically induced streaming.

We have successfully performed sono-optical manipulation of various types of samples (starch particles, pollen grains, uni-cellular organisms, cell clusters, cancer spheroids and more) of sizes up to 350  $\mu\text{m}$ , using forces per particle volume roughly around 0.1  $\text{pN } \mu\text{m}^{-3}$ , and achievable rotation rates of 0.1 Hz to 2 Hz. Controlled reorientation in all 3 directions was demonstrated on an elongated starch granule, and then sustained rotation, where the rotation axis and rate are controlled by the relative driving strength of the transducers, on a  $\sim 125 \mu\text{m}$  pollen grain. In another example,  $T_{\text{visc}}$  being only slightly larger than  $T_{\text{rad}}$  led to highly non-uniform rotations rates, with the particle spending a much longer time in one orientation than in others. Tracking a small feature on the particle in a recorded sinogram and fitting the curve to an orbiting motion with an angle-dependent and a uniform contribution provided a way to estimate the ratio of the two torque contributions.

The next step towards long-term biological monitoring will be to adapt the device to the respective requirements (such as temperature control, sterility, options for gas exchange), and afterwards dedicated biocompatibility assays will have to be carried out. But since the pressure amplitudes and forces we are applying do not exceed the commonly used levels, we anticipate no adverse effects.<sup>12,14</sup> We believe that our novel sono-optical approach will greatly facilitate the qualitative and quantitative assessments of suspended cell clusters, cancer spheroids and organoids, and possibly make a contribution towards reducing the necessary number of screening experiments on animals.

## Author contributions

Conceptualization, M. K. L., B. P., G. T., M. R. M.; methodology, M. K. L., B. P., G. T., M. R. M.; investigation, M. K. L. B. P.; formal analysis, M. K. L., B. P.; software, B. P., G. T., M. R. M.; writing – original draft, M. K. L., B. P., G. T., M. R. M.; writing – review & editing, G. T., M. R. M.; funding acquisition, M. R. M.; supervision, B. P., M. R. M., G. T.

## Conflicts of interest

No conflicts to declare.

## Acknowledgements

This work was supported by the Austrian Science Fund (FWF) under SFB-grant F68 *Tomography across the scales* (sub-project F6806-N36 Inverse Problems in Imaging of Trapped Particles). GT acknowledges support by the FWF grant P29936-N36. We thank Mike MacDonald (University of Dundee) for providing us with the optically transparent transducers. We thank Judith Hagenbuchner and Michael Ausserlechner (both Medical University Innsbruck) for providing us with the

spheroids. Additionally, we would like to thank Theresa Hofmann for laboratory assistance.

## Notes and references

- W. Mueller-Klieser, *J. Cancer Res. Clin. Oncol.*, 1987, **113**, 101–122.
- M. A. Lancaster, M. Renner, C.-A. Martin, D. Wenzel, L. S. Bicknell, M. E. Hurles, T. Homfray, J. M. Penninger, A. P. Jackson and J. A. Knoblich, *Nature*, 2013, **501**, 373–379.
- N. Sachs and H. Clevers, *Curr. Opin. Genet. Dev.*, 2014, **24**, 68–73.
- A. Ashkin, J. M. Dziedzic, J. E. Bjorkholm and S. Chu, *Opt. Lett.*, 1986, **11**, 288–290.
- A. Ashkin, J. M. Dziedzic and T. Yamane, *Nature*, 1987, **330**, 769–771.
- J. E. Curtis, B. A. Koss and D. G. Grier, *Opt. Commun.*, 2002, **207**, 169–175.
- D. A. Grier, *Nature*, 2003, **424**, 810–816.
- J. Leach, G. Sinclair, P. Jordan, J. Courtial, M. J. Padgett, J. Cooper and Z. J. Laczik, *Opt. Express*, 2004, **12**, 220–226.
- M. Padgett and R. Di Leonardo, *Lab Chip*, 2011, **11**, 1196–1205.
- G. Thalhammer, R. Steiger, S. Bernet and M. Ritsch-Marte, *J. Opt.*, 2011, **13**, 044024.
- Z. Yang, K. L. H. Cole, Y. Qiu, I. M. L. Somorjai, P. Wijesinghe, J. Nylk, S. Cochran, G. C. Spalding, D. A. Lyons and K. Dholakia, *Nat. Commun.*, 2019, **10**, 669.
- K. Dholakia, B. W. Drinkwater and M. Ritsch-Marte, *Nat. Rev. Phys.*, 2020, 1–12.
- L. P. Gor'kov, *Dokl. Akad. Nauk SSSR*, 1961, **140**, 88–92.
- M. Wiklund, *Lab Chip*, 2012, **12**, 2018–2028.
- S. Oberti, A. Neild and J. Dual, *J. Acoust. Soc. Am.*, 2006, **121**, 778.
- F. Guo, Z. Mao, Y. Chen, Z. Xie, J. P. Lata, P. Li, L. Ren, J. Liu, J. Yang, M. Dao, S. Suresh and T. J. Huang, *Proc. Natl. Acad. Sci. U. S. A.*, 2016, **113**, 1522–1527.
- Z. Tian, S. Yang, P.-H. Huang, Z. Wang, P. Zhang, Y. Gu, H. Bachman, C. Chen, M. Wu and Y. Xie, *et al.*, *Sci. Adv.*, 2019, **5**, eaau6062.
- X. Hu, J. Zhu, Y. Zuo, D. Yang, J. Zhang, Y. Cheng and Y. Yang, *Lab Chip*, 2020, **20**, 3515–3523.
- C. R. P. Courtney, C. E. M. Demore, H. Wu, A. Grinenko, P. D. Wilcox, S. Cochran and B. W. Drinkwater, *Appl. Phys. Lett.*, 2014, **104**, 154103.
- A. Franklin, A. Marzo, R. Malkin and B. W. Drinkwater, *Appl. Phys. Lett.*, 2017, **111**, 094101.
- L. Schmid, D. A. Weitz and T. Franke, *Lab Chip*, 2014, **14**, 3710–3718.
- K. W. Cheng, L. Alhasan, A. R. Rezk, A. Al-Abboodi, P. Doran, L. Y. Yeo and P. P. Y. Chan, *Biofabrication*, 2020, **12**, 015013.
- A. Marzo, S. A. Seah, B. W. Drinkwater, D. R. Sahoo and B. L. ad Sriram Subramanian, *Nat. Commun.*, 2015, **6**, 8661.
- A. Marzo and B. W. Drinkwater, *Proc. Natl. Acad. Sci. U. S. A.*, 2018, **116**, 84–89.
- M. Gedge and M. Hill, *Lab Chip*, 2012, **12**, 2998–3007.



- 26 C. Fury, C. Harfield, P. H. Jones, E. Stride and G. Memoli, Experimental characterisation of holographic optical traps for microbubbles, in *Nanophotonics V*, International Society for Optics and Photonics, 2014, vol. 9126, p. 91263L.
- 27 G. Thalhammer, C. McDougall, M. P. MacDonald and M. Ritsch-Marte, *Lab Chip*, 2016, **16**, 1523–1532.
- 28 G. Memoli, C. R. Fury, K. O. Baxter, P. N. Gálatc and P. H. Jones, *J. Acoust. Soc. Am.*, 2017, **141**, 3364.
- 29 A. Lamprecht, S. Lakämper, T. Baasch, I. A. Schaap and J. Dual, *Lab Chip*, 2016, **16**, 2682–2693.
- 30 P. Glynne-Jones and M. Hill, *Lab Chip*, 2013, **13**, 1003–1010.
- 31 X. Hu, H. Liu, Y. Jin, L. Liang, D. Zhu, X. Zhu, S. Guo, F. Zhou and Y. Yang, *Lab Chip*, 2018, **18**, 3405–3412.
- 32 G. W. J. Brodie, Y. Qiu, S. Cochran, G. C. Spalding and M. P. Macdonald, *IEEE Trans. Ultrason. Ferroelectr. Freq. Control*, 2014, **61**, 389–391.
- 33 O. Manneberg, J. Svennebring, H. M. Hertz and M. Wiklund, *J. Micromech. Microeng.*, 2008, **18**, 095025.
- 34 H. Bruus, *Lab Chip*, 2012, **12**, 20–28.
- 35 N. C. Dalrymple, S. R. Prasad, M. W. Freckleton and K. N. Chintapalli, *Radiographics*, 2005, **25**, 1409–1428.
- 36 L. Zhang and P. L. Marston, *Phys. Rev. E: Stat., Nonlinear, Soft Matter Phys.*, 2011, **84**, 065601.
- 37 K. Y. Bliokh and F. Nori, *Phys. Rev. B*, 2019, **99**, 174310.
- 38 J. Wu, *Fluids*, 2018, **3**, 108.
- 39 J. S. Bach and H. Bruus, *Phys. Rev. E*, 2019, **100**, 023104.
- 40 M. Wiklund, R. Green and M. Ohlin, *Lab Chip*, 2012, **12**, 2438–2451.
- 41 H. He, M. Friese, N. Heckenberg and H. Rubinsztein-Dunlop, *Phys. Rev. Lett.*, 1995, **75**, 826.
- 42 M. Padgett and R. Bowman, *Nat. Photonics*, 2011, **5**, 343–348.
- 43 T. A. Nieminen, T. Asavei, V. L. Loke, N. R. Heckenberg and H. Rubinsztein-Dunlop, *J. Quant. Spectrosc. Radiat. Transfer*, 2009, **110**, 1472–1482.
- 44 O. Brzobohatý, A. V. Arzola, M. Šiler, L. Chvátal, P. Ják, S. Simpson and P. Zemánek, *Opt. Express*, 2015, **23**, 7273–7287.
- 45 T. Asavei, V. L. Loke, M. Barbieri, T. A. Nieminen, N. R. Heckenberg and H. Rubinsztein-Dunlop, *New J. Phys.*, 2009, **11**, 093021.
- 46 G. Maidanik, *J. Acoust. Soc. Am.*, 1958, **30**, 620–623.
- 47 G. T. Silva, T. P. Lobo and F. G. Mitri, *EPL*, 2012, **97**, 54003.
- 48 Z. Fan, D. Mei, K. Yang and Z. Chen, *J. Acoust. Soc. Am.*, 2008, **124**, 2727.
- 49 T. Schwarz, P. Hahn, G. Petit-Pierre and J. Dual, *Microfluid. Nanofluid.*, 2015, **18**, 65–79.
- 50 J. P. Leao-Neto, J. H. Lopes and G. T. Silva, Acoustic radiation torque exerted on a subwavelength spheroidal particle by a traveling and standing plane wave, 2019, arXiv:1912.12933.
- 51 F. Mitri, T. Lobo and G. Silva, *Phys. Rev. E: Stat., Nonlinear, Soft Matter Phys.*, 2012, **85**, 026602.
- 52 H. Bruus, *Lab Chip*, 2012, **12**, 1014–1021.
- 53 T. Wang, H. Kanber and I. Rudnick, *Phys. Rev. Lett.*, 1977, **38**, 128.
- 54 P. B. Muller, R. Barnkob, M. J. H. Jensen and H. Bruus, *Lab Chip*, 2012, **12**, 4617–4627.
- 55 P. Hahn, I. Leibacher, T. Baasch and J. Dual, *Lab Chip*, 2015, **15**, 4302–4313.
- 56 A. Lamprecht, T. Schwarz, J. Wang and J. Dual, *J. Acoust. Soc. Am.*, 2015, **138**, 23–32.
- 57 P. L. Marston, *Proceedings of Meetings on Acoustics ICA2013*, 2013, p. 045005.
- 58 L. Zhang and P. L. Marston, *J. Acoust. Soc. Am.*, 2014, **136**, 2917–2921.
- 59 T. Schwarz, G. Petit-Pierre and J. Dual, *J. Acoust. Soc. Am.*, 2013, **133**, 1260–1268.
- 60 S. Deng, K. Jia, E. Wu, X. Hu, Z. Fan and K. Yang, *Appl. Sci.*, 2018, **8**, 73.
- 61 Q. Tang, F. Liang, L. Huang, P. Zhao and W. Wang, *Biomed. Microdevices*, 2020, **22**, 1–11.
- 62 G. Memoli, K. O. Baxter, H. G. Jones, K. P. Mingard and B. Zeqiri, *Micromachines*, 2018, **9**, 404.
- 63 N. Cardenas and S. K. Mohanty, *Appl. Phys. Lett.*, 2013, **103**, 013703.
- 64 M. Habaza, B. Gilboa, Y. Roichman and N. T. Shaked, *Opt. Lett.*, 2015, **40**, 1881–1884.
- 65 Y.-c. Lin, H.-C. Chen, H.-Y. Tu, C.-Y. Liu and C.-J. Cheng, *Opt. Lett.*, 2017, **42**, 1321–1324.
- 66 K. Kim, J. Yoon and Y. Park, *Optica*, 2015, **2**, 343–346.
- 67 K. Kim and Y. Park, *Nat. Commun.*, 2017, **8**, 1–8.
- 68 G. Thalhammer, R. Steiger, M. Meinschad, M. Hill, S. Bernet and M. Ritsch-Marte, *Biomed. Opt. Express*, 2011, **2**, 2859.
- 69 J. Hagenbuchner, U. Kiechl-Kohlendorfer, P. Obexer and M. Ausserlechner, *Oncogene*, 2016, **35**, 2052.
- 70 J. Hagenbuchner, V. Obsilova, T. Kaserer, N. Kaiser, B. Rass, K. Psenakova, V. Docekal, M. Alblova, K. Kohoutova and D. Schuster, *et al.*, *eLife*, 2019, **8**, e48876.
- 71 S. Kumar, M. Gunaseelan, R. Vaippully, A. Kumar, M. Ajith, G. Vaidya, S. Dutta and B. Roy, *Biomed. Opt. Express*, 2020, **11**, 3555–3566.

